

Supplementary Materials for

Jupiter's interior and deep atmosphere: The initial pole-to-pole passes with the Juno spacecraft

S. J. Bolton,* A. Adriani, V. Adumitroaie, M. Allison, J. Anderson, S. Atreya, J. Bloxham, S. Brown, J. E. P. Connerney, E. DeJong, W. Folkner, D. Gautier, D. Grassi, S. Gulkis, T. Guillot, C. Hansen, W. B. Hubbard, L. Iess, A. Ingersoll, M. Janssen, J. Jorgensen, Y. Kaspi, S. M. Levin, C. Li, J. Lunine, Y. Miguel, A. Mura, G. Orton, T. Owen, M. Ravine, E. Smith, P. Steffes, E. Stone, D. Stevenson, R. Thorne, J. Waite, D. Durante, R. W. Ebert, T. K. Greathouse, V. Hue, M. Parisi, J. R. Szalay, R. Wilson

*Corresponding author. Email: sbolton@swri.edu

Published 26 May 2017, *Science* **356**, 821 (2017)
DOI: 10.1126/science.aal2108

This PDF file includes:

Materials and Methods

Figs. S1 to S4

Tables S1 to S4

References

Materials and Methods

Microwave Radiometer

The Juno Microwave Radiometer (MWR) comprises six separate radiometers (channels 1-6) that operate at frequencies distributed approximately by octave from 600 MHz to 22 GHz (50 to 1.2 cm wavelength) respectively, as listed in Table S1. Each channel obtains contiguous measurements of the antenna temperature T_a at 100-ms intervals with the uncertainties given in the table. Since the spacecraft spins at 2 rotations per minute, observations are taken at spacecraft clock angle increments of 1.2° . Given the antenna beamwidths in the table, this amounts to 10 or more observations per MWR footprint on Jupiter. Allowing for averaging of adjacent measurements and the typical source temperature at each wavelength, the intrinsic instrument noise in the nadir brightness temperatures shown in Figure 2 are negligible compared to the relative and absolute errors of 0.1% and 2% respectively.

At the longest-wavelength channels, particularly channel 1, synchrotron emission from Jupiter's radiation belts becomes particularly strong and contamination of atmospheric measurements due to radiation from this source entering the antenna sidelobes must be corrected. Particular care in the design and implementation of the antennas was taken to minimize this source of error so that it does not limit our ability to measure the nadir brightness and its emission angle dependence. Figure S1 shows a validation of the design using data obtained during the PJ1 pass. This plot shows the calibrated antenna temperature obtained as a function of spacecraft clock angle with respect to nadir for channel 1, with the emission from both sources shown in context. Each horizontal line in the figure represents the contiguous antenna temperature measurements obtained during one rotation of the spacecraft as it sweeps from north to south across Jupiter, crossing closest to nadir at 0° clock angle, then sweeping around across the radiation belt in the opposite hemisphere. The vertical shape symmetric about 0° deg clock angle is Jupiter's thermal emission, while the bright signal in the rest of the sky is the synchrotron emission. The spurs of synchrotron radiation that begin to impinge on the planet near $\pm 40^\circ$ latitudes correspond to the north and south horns of radiation from mirror-point electrons that come close to the spacecraft at these latitudes. The separation of thermal atmospheric radiation from synchrotron emission appears complete in this image, although detailed calculations using the known antenna beam pattern show that a small contribution from the latter remains at the nadir line (12). Nevertheless this contributes less than 1% to the atmospheric signal and is negligible for the nadir brightness analysis reported here, although the effect on emission angle dependence has not been corrected. The rapid decrease of the synchrotron emission with decreasing wavelength makes it negligible for nadir emissions in all other channels.

The calculations used to interpret the measurements make use of the Juno Atmospheric Microwave Radiative Transfer (JAMRT) code developed by the Juno project for this purpose (12). Combined with a model of the atmosphere, JAMRT computes radiances from profiles of temperature, ammonia and water from the cloud tops down to pressures of 1000 bars. The model uses experimental data on the opacity of ammonia and water in hydrogen-helium mixtures at temperatures up to 600 K and pressures up to 100 bars (18,

41-43). The uncertainties of the opacity models have been determined to be about 5% to 7% from low pressures up to 100 bars. These determinations are supplemented by room-temperature data that range to several hundred bars (44). The model allows for variations in pressure-temperature structure, variable concentrations of constituents in addition to water and ammonia gas that affect the opacity such as water/ammonia cloud droplets and NH_4SH (from H_2S reacting with NH_3). All brightness temperatures are computed assuming a one-dimensional line-of-sight integration from above the atmosphere with no scattering or refraction.

Figure S2 shows the brightness temperature contribution functions computed for the six MWR channels using JAMRT and an assumed atmosphere containing nominal concentrations of ammonia and water ($3 \times$ solar each), each assumed to be uniformly mixed up to their respective saturation levels and following a saturation curve above that. The contribution function is calculated here as the fractional contribution to the net brightness temperature per increment of $\log(P)$, so that the area under the curve for a given pressure range is proportional to the net thermal contribution from that range. The contribution functions are approximately symmetric in $\log(P)$ for channels 2 through 6 (24 to 1.37 cm), with peaks around 30, 10, 3.5, 1.5 and 0.7 bars respectively, and are generally contained within the region where the opacities of NH_3 and H_2O have been measured. The highest frequency lies in the center of the strong ammonia 1-cm band, and the remaining frequencies were chosen to provide overlapping weighting functions descending as far as feasible into Jupiter's depths. However, most of the contribution to channel 1 brightness temperatures depends on extrapolation by as much as two orders of magnitude in pressure beyond the range of laboratory measurements, and to temperatures in excess of 2000 K. While structure seen at this lowest frequency indicates very deep dynamics, its interpretation will have a different character than that from the other channels because the opacity at depth is more uncertain.

Comparison of PJ1 and PJ3 brightnesses indicates that longitudinal variations are further confined to a "weather layer" at pressures less than about 9 bars. The results are qualitatively consistent with the Galileo probe results, which have low values of the ammonia mixing ratio extending well below the ammonia cloud and then transitioning to a higher value deeper down. Figure 3 shows the transition occurring at a pressure of ~ 25 bar, but this is deeper by a factor of 3 in pressure than that observed by the Galileo probe. Juno's value for the NH_3 mixing ratio at 200 bars is 330-370 ppmv, whereas absorption of the Galileo probe radio signal gives 700 ± 100 ppmv, and the Galileo probe mass spectrometer gives 568 ± 215 ppmv (where we have converted from values relative to H_2 to those relative to the bulk mixture). The unexpected concentrations measured by the Galileo probe for both NH_3 and H_2O have been ascribed to its landing in an anomalous atmospheric region (a 5-micron hot spot). In the context of our results, we note that the probe descended into the atmosphere at 7°N just at the transition between the equatorial plume and the NEB ammonia-dry region, where the measurements would be expected to depend strongly on the exact location. This general location is a region of intermixed ascending ammonia-rich and descending ammonia-poor gas, and a single measurement cannot be expected to give a representative picture of Jupiter's composition for condensable gasses.

In inverting the data in Fig. 2, we assumed that the horizontal variations of brightness temperature are due to horizontal variations of opacity, i.e., ammonia, rather than horizontal variations of temperature. The rationale for this assumption is that real temperature variations $\Delta T(y, P)$, i.e., temperature variations at constant pressure, would lead to impossibly large wind speeds. Winds are connected to temperatures by the thermal wind equation

$$f \frac{\partial \bar{u}}{\partial \log P} = R \left(\frac{\partial T}{\partial y} \right)_P \quad (S1)$$

Here f is the Coriolis parameter, \bar{u} is the mean eastward velocity, R is the gas constant for the hydrogen-helium atmosphere, and y is the northward coordinate measured from the equator. This equation is valid when the horizontal dimensions of interest are much greater than the vertical dimensions, as they are in Fig. 3. Close to the equator f is equal to βy , where $\beta = 2\Omega/a$, Ω is the rotation rate, and a is the radius of the planet. We fit the brightness temperatures in Fig. 2 to a Gaussian of the form $T(y, P) = \Delta T \exp(-y^2/y_0^2)$, where $\Delta T = -40$ K and $y_0 = 5000$ km, about 4° of latitude. Left and right sides of Equation (1) vanish at the equator, so we use L'Hôpital's rule to obtain

$$\frac{\partial \bar{u}}{\partial \log P} = -\frac{2R\Delta T}{\beta y_0^2} \approx 2350 \text{ m s}^{-1} \quad (S2)$$

Distributed over $\log P = 4.6$, about 2 orders of magnitude in P , the velocity at the top relative to that at the bottom of Fig. 3 would be -10800 m s^{-1} , which is impossibly large and of the wrong sign. Thus the brightness temperature differences cannot be due to $\Delta T(y, P)$ and must be due to opacity variations.

Gravity Field

Mission orbit geometry and gravity data

Key geometry information for the first two Juno perijoves following orbit insertion, designated PJ1 and PJ2, are given in Table S2. The orbit was nearly polar with orbit period 53 days. The time of perijove is given in barycentric dynamical time (TDB). The orbit plane was nearly perpendicular to the direction from Earth to Jupiter. Both perijoves were near solar conjunction. At perijove the height of the spacecraft above the 1-bar ellipsoid was about 4100 km at latitude 3.8° N and 4.7° N. The spacecraft was nearly over the north pole of Jupiter about one hour before perijove and above the south pole about one hour after perijove. When above the north and south poles the spacecraft was approximately one Jupiter radius above the 1-bar level.

For PJ1 the data used cover from 3.2 hours before perijove to 5.1 hours after perijove. For PJ2 the data covered from 3.1 hours before perijove to 2.8 hours after perijove. For both perijoves, the tracking station transmitted a radio signal to the spacecraft at X-band (8 GHz). A transponder on the spacecraft locked coherently in phase

onto the signal from the tracking station and transmitted a signal back to the tracking station.

For PJ1 the spacecraft transmitted signals at both X-band and at Ka band (32 GHz). The difference in the Doppler shift of the X-band and Ka-band signals were used to calibrate the effect of charged particles on the radio signal from the spacecraft to Earth. The only significant signature in this calibration is near the time of closest approach to Jupiter. Near perijove the spacecraft was inside the orbit of Io and the radio signal passed through the Io plasma torus. The Io plasma torus causes an effect on radio signals that has been previously measured from the Voyager and Ulysses spacecraft (45, 46). We used the dual-frequency radio signal to Earth to calibrate the effect of the plasma torus, also applied, appropriately scaled, to the X-band radio signal from the tracking station to the spacecraft. We applied an estimate of the effect of the Io plasma torus to the PJ2 data based on the dual-frequency measurements from PJ1.

The data noise for PJ1 was dominated by a combination of fluctuations in the troposphere and antenna mechanical noise. The data noise for PJ2 was dominated by solar plasma but at lower level than expected (47). The measurement noise for the two orbits is characterized by the Allan deviation (48) that measures the fractional frequency stability as a function of the integration time. For the Jovian gravity field estimation the main time scales of interest are from ~ 100 s to ~ 1000 s, for which the change in Doppler is caused by the zonal gravity harmonics from degree 2 to degree 12. Figures S3 and S4 show the Allan deviation for Doppler residuals. These are based on residuals after estimation of the relevant parameters. Data from the hour centered on perijove are excluded, since over that time the estimated parameters can absorb some of the measurement noise. The slope of the Allan deviation for PJ1 residuals over 100 s to 1000 s indicates white frequency noise, while for PJ2 the slope of Allan deviation indicates noise dominated by solar plasma. For PJ1 the slope of the Allan deviation indicates the Doppler measurements as a function of time are uncorrelated, while for PJ2 the Doppler measurements at different times have non-zero correlation as a function of the time between point. This correlation function can be calculated to provide the correct data weighting to use for estimation.

Gravity model and estimation technique

The mass distribution of a planet is generally different from that of a homogeneous spherical body. For this reason, the external gravitational potential of Jupiter can be conveniently expanded in series of spherical harmonics of degree l and order m (49):

$$U(r, \lambda, \phi) = \frac{GM}{r} \sum_{n=0}^{\infty} \sum_{m=0}^n \left(\frac{R}{r}\right)^n P_{nm}(\sin \phi) [C_{nm} \cos(m\lambda) + S_{nm} \sin(m\lambda)] \quad (S3)$$

where G is the gravitational constant, M and R are the mass and radius of Jupiter, r is the distance from Jupiter's center of mass, ϕ is the latitude, λ is the longitude, P_{nm} are the un-normalized associated Legendre functions, and C_{nm} and S_{nm} are the un-normalized spherical harmonic coefficients. The gravitational acceleration affecting the trajectory of Juno while orbiting about Jupiter can be calculated by taking the gradient of the

gravitational potential. In turn, spherical harmonics can be estimated by precise Doppler tracking of the spacecraft along with other relevant parameters.

The state vector x is the set of the estimated parameters. By means of radiometric observables z , it is possible to obtain a least-squares estimate x_c of the state vector, designed to combine a priori information and new data (50):

$$x_c = (A^T W A + \tilde{\Lambda})^{-1} (A^T W z + \tilde{\Lambda} \tilde{x}) \quad (\text{S4})$$

where A is the matrix of observation partials, W is the observable weighting matrix, $\tilde{\Lambda}$ is the a priori information matrix and \tilde{x} is an unbiased *a priori* estimate of the state vector. The quantity P_x , given by:

$$P_x = (A^T W A + \tilde{\Lambda})^{-1} \quad (\text{S5})$$

is the covariance matrix, which bears information about the estimation accuracies. The square roots of the diagonal elements correspond to the formal uncertainties on the estimated parameters.

The measurements used for gravity analysis allow the estimation of a limited number of parameters, supported by the available data strength. However, unestimated parameters (for instance higher degree and order gravity harmonics) can be dynamically correlated with the estimated parameters and might undermine the filter accuracy and confidence in the estimated values and covariance.

One strategy to prevent the underestimation of the covariance is the technique of consider analysis. This approach features a set of parameters y which are not estimated, but whose a priori covariance P_y is used to augment the least-squares uncertainty. The consider covariance P_{CON} is given by:

$$P_{CON} = P_x + S P_y S^T \quad (\text{S6})$$

where S is the sensitivity matrix:

$$S = \partial(x - x_c)/\partial y \quad (\text{S7})$$

where $x - x_c$ is the difference between the true value of x and the least-squares estimate x_c . The consider covariance is composed of two positive definite terms: (i) the standard covariance matrix P_x ; (ii) an additional component which depends on the sensitivity matrix and the a priori covariance for the consider parameters.

When data is accumulated (i.e. data available for more than one perijove) it is possible to adopt a multi-arc approach (51), where the information from different arcs is combined. In this case, the formal uncertainties P_x will decrease because of the higher information content, while consider covariance P_{CON} can sometimes increase when estimated parameters are highly correlated with unestimated parameters.

Jovian gravity field estimation

The Doppler data from PJ1 and PJ2 were used to estimate the Jovian gravity field parameterized by zonal harmonics through degree 12 plus sectoral and tesseral harmonics of degree 2 along with corrections to the Jupiter spin axis direction and the initial position and velocity of the spacecraft for each perijove. The Juno data have less sensitivity to the Jupiter mass parameter (GM) than the data from the Galileo orbiter flybys of the Galilean satellites. We have applied a constraint to the Jupiter GM based on a fit to the Galileo orbiter data (24). The a priori uncertainties for the other estimated parameters were set to be large compared with the final estimated uncertainties. The Jovian gravity field is also affected by tides raised by the Jovian satellites, with largest contribution by Io. Because the longitude of Juno with respect to Io was almost the same for PJ1 and PJ2 the data are not able to separate tide signature. Instead we have modeled the effect of tides using a value for the k_2 Love number of 0.379 from *Gavrilov and Zharkov* (52). The tide model adds a time-averaged corrections $\Delta J_2 = 0.054 \times 10^{-6}$ and $\Delta C_{22} = 0.026 \times 10^{-6}$ that are small compared with the estimated uncertainties in J_2 and C_{22} .

The estimated gravity parameters are given in Table S3. The correlations between parameters are given in Table S4. The odd zonal parameters for degree greater than 3 along with J_{10} and J_{12} are not included in Table S3 since the estimated values are well below the uncertainties. The uncertainties listed account for both the effect of the observed data noise and from possible systematic errors using the consider analysis described above. The uncertainties include the effect of consider parameters describing a possible gravity field of degree and order 30 due to surface winds with depth of 10,000 km (53). This results in gravity coefficient uncertainties that are fairly conservative but not an upper bound. The winds speeds used for this model are observed at the cloud tops, while to deeper winds may be larger. The only observation of Jovian wind speeds below the cloud levels from the Galileo probe were significantly larger than the cloud-top winds (54).

The estimated values of the degree two sectoral and tesseral coefficients are well below the uncertainties. The values of C_{21} and S_{21} are zero if Jupiter's principal axis of inertia coincides with the spin axis. The values of C_{22} and S_{22} are zero if the mass distribution is symmetric about the rotation axis. These properties are expected for the fluid planet in equilibrium and have been used as constraints in some earlier analyses. The Juno data are strong enough to confirm these expectations.

Hot Spots

Starting from the preparatory work for the analysis of the JIRAM data from Grassi et al. (55), an end-to-end retrieval code based on the Bayesian formalism (56) was developed. The code is intended to study the composition of the upper troposphere in the pressure range 1-6 bars in Jupiter areas where a moderate cloud optical thickness ($\tau < 2$) allows the thermal radiation to be emitted in this pressure range for measurements from space. The present code also includes a forward radiative transfer model based on correlated-k method (57). Multiple scattering by clouds is also taken into account through a simple two-streams approach (58).

The water, ammonia and phosphine abundances derived from JIRAM Hot Spot data reinforce the current view of the brightest parts of these areas as sites of prevailing descending vertical motions (59). Nonetheless, possible evidence of upwelling is observed at the southern boundaries, as local enrichments in ammonia and phosphine along latitude rather than strictly correlated with $5\mu\text{m}$ radiance. Local minima of water relative humidity are also tentatively identified eastward of Hot Spot brightest parts, suggesting that Hot Spot IR morphology can be altered by clouds located higher than the 1.3-1 bar level assumed for the residual layer of ammonium hydrosulfide, consistently with the spacecraft visible observations discussed by (60) and (61).

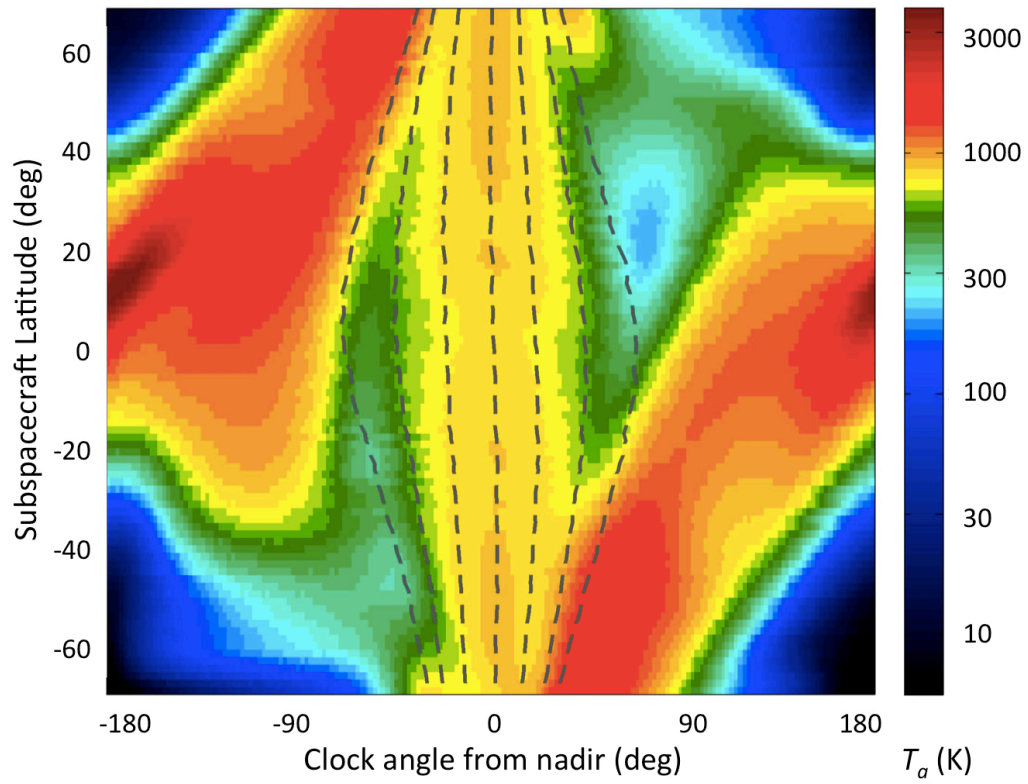


Fig. S1.

Channel 1 antenna temperature as a function of spacecraft clock angle through the perijove 1 pass. The dashed lines indicate lines of constant incidence angle at 0, 30, 60 and 90 degrees.

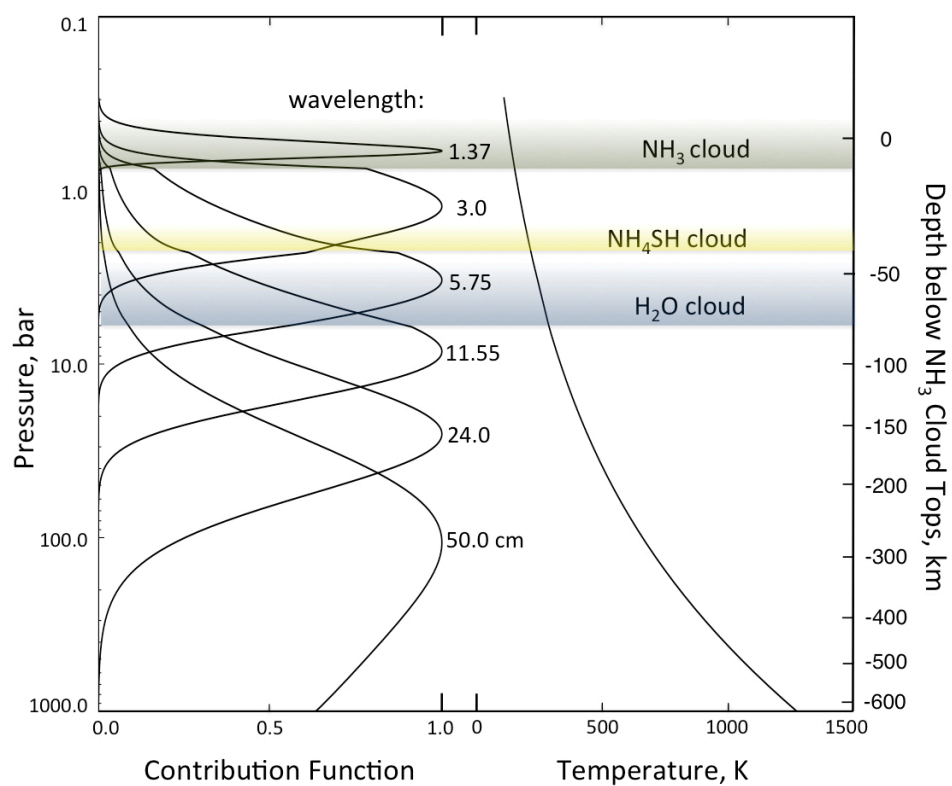


Fig. S2

Contribution functions for a nominal Jovian atmosphere at the MWR wavelengths and points for laboratory measurements of NH_3 and H_2O microwave opacity in context with a Jovian pressure-temperature profile.

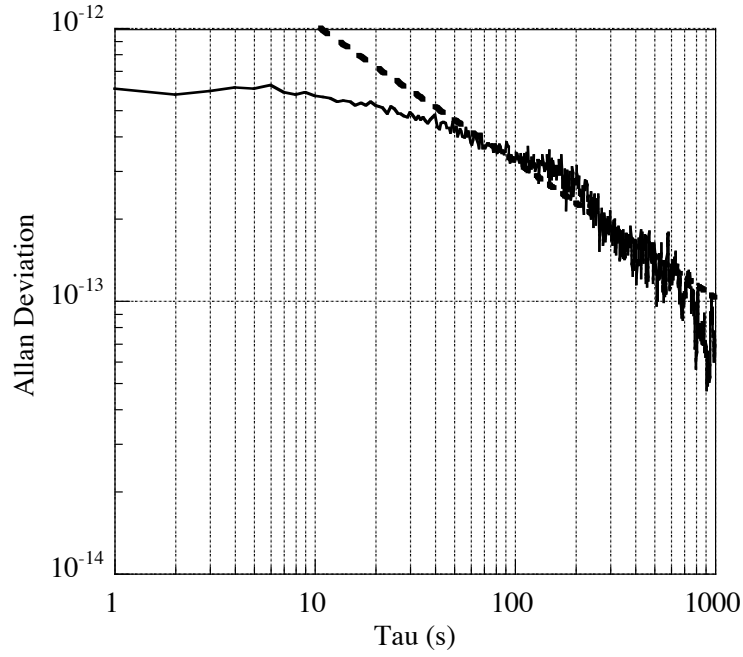


Fig. S3

The Allan deviation of the Doppler measurements from PJ1. For time scales from 100 to 1000 seconds the slope is approximately proportional to $\tau^{-1/2}$ (dashed line) indicating the Doppler measurements are independent for those time scale.

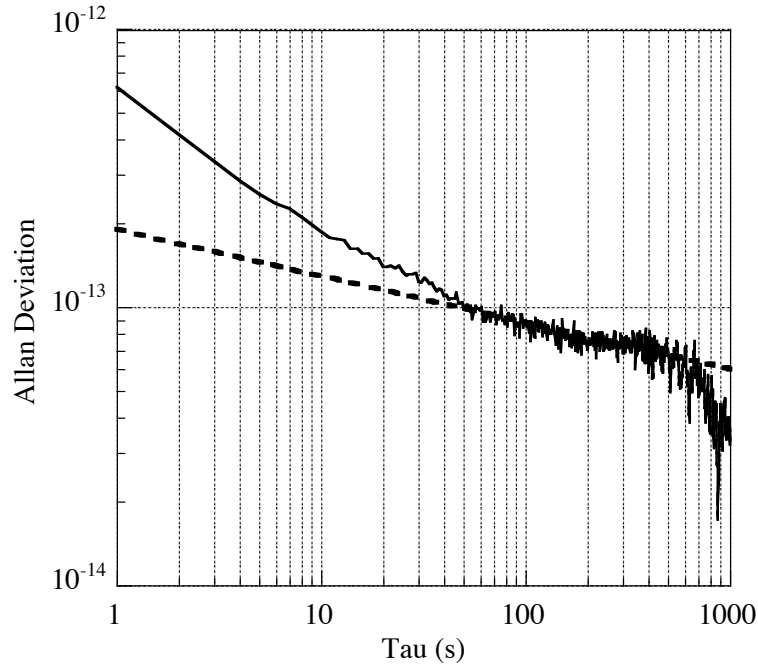


Fig. S4

The Allan deviation of the Doppler measurements from PJ2. For time scales from 100 to 1000 seconds the slope is approximately proportional to $\tau^{-1/6}$ (dashed line) indicating the Doppler measurements are correlated on those time scales due to the character of solar plasma.

Table S1.

MWR antenna and receiver characteristics. ΔT_{noise} is the typical noise temperature for a 100 ms integration.

Channel	Frequency [GHz]	Wavelength [cm]	Beamwidth [deg]	ΔT_{noise} (100 ms) [K]
1	0.600	50	20.6°	0.59
2	1.248	24	21.0°	0.54
3	2.597	11.55	12.1°	0.42
4	5.215	5.75	12.1°	0.39
5	10.004	3.0	12.0°	0.21
6	21.900	1.37	10.8°	0.19

Table S2.

Geometry information for perijoves 1 and 2, including time of perijove, one-way light travel time LT from spacecraft to Earth, distance d from Juno to Earth, inclination i , of the orbit plane to Jupiter equator, height above Jupiter 1-bar ellipsoid at perijove h , latitude l , of perijove, angle b between orbit normal and direction from Earth to Jupiter, and angular separation SEP between the Sun and Jupiter as seen from Earth.

PJ	Time (TDB)	LT(min)	d (au)	i ($^{\circ}$)	h (km)	λ ($^{\circ}$)	β ($^{\circ}$)	SEP($^{\circ}$)
1	2016 August 27 12:51:52	53.0	6.37	89.9	4147	3.8	2.8	22.6
2	2016 October 19 18:12:02	53.1	6.39	90.0	4179	4.7	9.4	18.2

Table S3.

Estimated Jovian gravity field parameters from Pioneer/Voyager and from Juno's first two science orbits combined. The zonal harmonics J_n and degree-2 tesseral harmonics S_{ij} and C_{ij} are unnormalized and dimensionless. The Jupiter spin axis direction given by Earth right ascension α and declination δ at epoch 2000.0. The gravity harmonics from Pioneer and Voyager have been scaled from the Jupiter radius they used to the radius 71492 km adopted by Juno, whilst their pole direction has been converted from Earth-Mean-Equator of 1950 to Earth-Mean-Equator of 2000.

Parameter	Pioneer/Voyager	Jup230	Jup310	Juno PJ1&PJ2
$GM(\text{km}^3/\text{s}^2)$	126686537.5 ± 101	126686534.9 ± 1.5	126686534.2 ± 2.7	126686533.0 ± 2.0
$J_2 \times 10^6$	14697.3 ± 1	14696.43 ± 0.21	14695.62 ± 0.29	14696.514 ± 0.272
$J_3 \times 10^6$	1.4 ± 5	-0.64 ± 0.90		-0.067 ± 0.458
$J_4 \times 10^6$	-583.9 ± 5	-587.14 ± 1.68	-591.31 ± 2.06	-586.623 ± 0.363
$J_6 \times 10^6$	30.8 ± 20	34.25 ± 5.22	20.78 ± 4.87	34.244 ± 0.236
$J_8 \times 10^6$				-2.502 ± 0.311
$C_{21} \times 10^6$				0.026 ± 0.303
$S_{21} \times 10^6$				0.030 ± 0.368
$C_{22} \times 10^6$	-0.030 ± 0.150	0.007 ± 0.008	-0.010 ± 0.067	0.005 ± 0.170
$S_{22} \times 10^6$	-0.007 ± 0.150	-0.013 ± 0.009	-0.014 ± 0.061	-0.010 ± 0.214
$\alpha(\text{deg})$	268.058 ± 0.005	268.0566 ± 0.0002	268.0571 ± 0.0003	268.057 ± 0.002
$\delta(\text{deg})$	64.494 ± 0.002	64.4953 ± 0.0001	64.4958 ± 0.0001	64.496 ± 0.013

Table S4.

Correlation matrix for estimated Jovian gravity field parameters. The correlation matrix is symmetric so only the upper diagonal is shown.

	RA0	DEC0	C21	S21
GM5	-1.50E-03	5.53E-03	3.74E-04	-7.78E-03
RA0		-8.28E-01	-9.82E-01	2.67E-01
DEC0			7.31E-01	-7.57E-01
C21				-1.26E-01

	S21	C22	S22	J2
GM5	-7.78E-03	-6.69E-03	-5.62E-03	-3.14E-03
RA0	2.67E-01	6.75E-01	8.32E-01	3.47E-01
DEC0	-7.57E-01	-9.61E-01	-9.95E-01	-4.77E-01
C21	-1.26E-01	-5.65E-01	-7.35E-01	-3.45E-01
S21		8.74E-01	7.48E-01	3.80E-01
C22			9.48E-01	5.00E-01
S22				4.72E-01
J2				

	J3	J4	J6	J8
GM5	5.61E-03	2.94E-03	4.22E-03	3.93E-03
RA0	-5.07E-01	-5.73E-01	-5.77E-01	-6.29E-01
DEC0	7.57E-01	5.70E-01	6.67E-01	6.87E-01
C21	4.44E-01	5.17E-01	4.84E-01	5.47E-01
S21	-7.62E-01	-3.62E-01	-5.14E-01	-4.85E-01
C22	-8.32E-01	-5.14E-01	-6.24E-01	-6.31E-01
S22	-7.51E-01	-6.18E-01	-7.13E-01	-7.30E-01
J2	-3.21E-01	-3.16E-01	-3.17E-01	-3.45E-01
J3		3.90E-01	4.23E-01	4.47E-01
J4			8.33E-01	8.63E-01
J6				9.27E-01

References

1. J. E. P. Connerney, A. Adriani, F. Allegrini, F. Bagenal, S. J. Bolton, B. Bonfond, S. W. H. Cowley, J.-C. Gerard, G. R. Gladstone, D. Grodent, G. Hospodarsky, J. L. Jorgensen, W. S. Kurth, S. M. Levin, B. Mauk, D. J. McComas, A. Mura, C. Paranicas, E. J. Smith, R. M. Thorne, P. Valek, J. Waite, Jupiter's magnetosphere and aurorae observed by the Juno spacecraft during its first polar orbits. *Science* **356**, 826 (2017).
2. C. J. Hansen, M. A. Caplinger, A. Ingersoll, M. A. Ravine, E. Jensen, S. Bolton, G. Orton, Junocam: Juno's outreach camera. *Space Sci. Rev.* 10.1007/s11214-014-0079-x (2014). [doi:10.1007/s11214-014-0079-x](https://doi.org/10.1007/s11214-014-0079-x)
3. T. Gehrels, in *Jupiter: Studies of the Interior, Atmosphere, Magnetosphere and Satellites*, T. Gehrels, Ed. (Univ. of Arizona Press, 1976), pp. 531–563.
4. E. García-Melendo, A. Sanchez-Lavega, A study of the stability of jovian zonal winds from HST images: 1995–2000. *Icarus* **152**, 316–330 (2001). [doi:10.1006/icar.2001.6646](https://doi.org/10.1006/icar.2001.6646)
5. X. S. Asay-Davis, P. S. Marcus, M. H. Wong, I. de Pater, Changes in Jupiter's zonal velocity between 1979 and 2008. *Icarus* **211**, 1215–1232 (2011). [doi:10.1016/j.icarus.2010.11.018](https://doi.org/10.1016/j.icarus.2010.11.018)
6. A. P. Ingersoll, R. F. Beebe, S. A. Collins, G. E. Hunt, J. L. Mitchell, P. Muller, B. A. Smith, R. J. Terrile, Zonal velocity and texture in the jovian atmosphere inferred from Voyager images. *Nature* **280**, 773–775 (1979). [doi:10.1038/280773a0](https://doi.org/10.1038/280773a0)
7. D. A. Godfrey, A hexagonal feature around Saturn's north pole. *Icarus* **76**, 335–356 (1988). [doi:10.1016/0019-1035\(88\)90075-9](https://doi.org/10.1016/0019-1035(88)90075-9)
8. N. Barrado-Izaguirre, S. Perez-Hoyos, A. Sanchez-Lavega, Brightness power spectral distribution and waves in Jupiter's upper cloud and hazes. *Icarus* **202**, 181–196 (2009). [doi:10.1016/j.icarus.2009.02.015](https://doi.org/10.1016/j.icarus.2009.02.015)
9. A. Antuñano, T. del Río-Gaztelurrutia, A. Sánchez-Lavega, R. Hueso, Dynamics of Saturn's polar regions. *J. Geophys. Res.* **120**, 155–176 (2015). [doi:10.1002/2014JE004709](https://doi.org/10.1002/2014JE004709)
10. U. A. Dyudina, A. P. Ingersoll, S. P. Ewald, A. R. Vasavada, R. A. West, K. H. Baines, T. W. Momary, A. D. Del Genio, J. M. Barbara, C. C. Porco, R. K. Achterberg, F. M. Flasar, A. A. Simon-Miller, L. N. Fletcher, Saturn's south polar vortex compared to other large vortices in the Solar System. *Icarus* **202**, 240–248 (2009). [doi:10.1016/j.icarus.2009.02.014](https://doi.org/10.1016/j.icarus.2009.02.014)
11. M. A. Janssen, M. Hofstadter, S. Gulkis, A. Ingersoll, M. Allison, S. Bolton, S. Levin, L. Kamp, Microwave remote sensing of Jupiter's atmosphere from an orbiting spacecraft. *Icarus* **173**, 447–453 (2005). [doi:10.1016/j.icarus.2004.08.012](https://doi.org/10.1016/j.icarus.2004.08.012)
12. M. A. Janssen, J. E. Oswald, S. T. Brown, S. Gulkis, S. M. Levin, S. J. Bolton, M. D. Allison, S. K. Atreya, D. Gautier, A. P. Ingersoll, J. I. Lunine, G. S. Orton, T. C. Owen, P. G. Steffes, V. Adumitroaie, A. Bellotti, L. A. Jewell, C. Li, L. Li, S. Misra, F. A.

- Oyafuso, D. Santos-Costaz, E. Sarkissian, R. Williamson, J. K. Arballo, A. Kitiyakaral, A. Ulloa-Severino, J. C. Chen, F. W. Maiwald, A. S. Sahakian, P. J. Pingree, K. A. Lee, A. S. Mazer, R. Redick, R. E. Hodges, R. C. Hughes, G. Bedrosian, D. E. Dawson, W. A. Hatch, D. S. Russell, N. F. Chamberlain, M. S. Zawadskil, B. Khayatianl, B. R. Franklin, H. A. Conley, J. G. Kempenaar, M. S. Lool, E. T. Sunada, V. Vorperion, C. C. Wang, MWR: Microwave radiometer for the Juno mission to Jupiter. *Space Sci. Rev.* 10.1007/s11214-017-0349-5 (2017). [doi:10.1007/s11214-017-0349-5](https://doi.org/10.1007/s11214-017-0349-5)
13. W. M. Folkner, R. Woo, S. Nandi, Ammonia abundance in Jupiter's atmosphere derived from the attenuation of the Galileo probe's radio signal. *J. Geophys. Res.* **103**, 22847–22855 (1998). [doi:10.1029/98JE01635](https://doi.org/10.1029/98JE01635)
 14. M. H. Wong, P. R. Mahaffy, S. K. Atreya, H. B. Niemann, T. C. Owen, Updated Galileo probe mass spectrometer measurements of carbon, oxygen, nitrogen, and sulfur on Jupiter. *Icarus* **171**, 153–170 (2004). [doi:10.1016/j.icarus.2004.04.010](https://doi.org/10.1016/j.icarus.2004.04.010)
 15. M. A. Janssen, Ed., *Atmospheric Remote Sensing by Microwave Radiometry* (Wiley, 1993).
 16. P. G. Steffes, T. R. Hanley, B. M. Karpowicz, K. Devaraj, S. Noorizadeh, D. Duong, G. Chinsomboon, A. Bellotti, Michael A. Janssen, S. J. Bolton, high-precision laboratory measurements supporting retrieval of water vapor, gaseous ammonia, and aqueous ammonia clouds with the Juno Microwave Radiometer (MWR). *Space Sci. Rev.* 10.1007/s11214-01600265-0 (2017). [doi:10.1007/s11214-01600265-0](https://doi.org/10.1007/s11214-01600265-0)
 17. C. Li, A. Ingersoll, M. Janssen, S. Levin, S. Bolton, V. Adumitroaie, M. Allison, J. Arballo, A. Bellotti, S. Brown, S. Ewald, L. Jewell, S. Misra, G. Orton, F. Oyafuso, P. Steffes, R. Williamson, The distribution of ammonia on Jupiter from a preliminary inversion of Juno Microwave Radiometer data. *Geophys. Res. Lett.* 10.1002/2017GL073159 (2017). [doi:10.1002/2017GL073159](https://doi.org/10.1002/2017GL073159)
 18. S. K. Atreya, A. S. Wong, K. H. Baines, M. H. Wong, T. C. Owen, Jupiter's ammonia clouds—localized or ubiquitous? *Planet. Space Sci.* **53**, 498–507 (2005). [doi:10.1016/j.pss.2004.04.002](https://doi.org/10.1016/j.pss.2004.04.002)
 19. A. Adriani, G. Filacchione, T. Di Iorio, D. Turrini, R. Noschese, A. Cicchetti, D. Grassi, A. Mura, G. Sindoni, M. Zambelli, G. Piccioni, M. T. Capria, F. Tosi, R. Orosei, B. M. Dinelli, M. L. Moriconi, E. Roncon, J. I. Lunine, H. N. Becker, A. Bini, A. Barbis, L. Calamai, C. Pasqui, S. Nencioni, M. Rossi, M. Lastri, R. Formaro, A. Olivieri, JIRAM, the Jovian Infrared Auroral Mapper. *Space Sci. Rev.* 10.1007/s11214-014-0094-y (2014). [doi:10.1007/s11214-014-0094-y](https://doi.org/10.1007/s11214-014-0094-y)
 20. B. A. Archinal, M. F. A'Hearn, E. Bowell, A. Conrad, G. J. Consolmagno, R. Courtin, T. Fukushima, D. Hestroffer, J. L. Hilton, G. A. Krasinsky, G. Neumann, J. Oberst, P. K. Seidelmann, P. Stooke, D. J. Tholen, P. C. Thomas, I. P. Williams, Report of the IAU

Working Group on Cartographic Coordinates and Rotational Elements: 2009. *Celestial Mech. Dyn. Astron.* **109**, 101–135 (2010). [doi:10.1007/s10569-010-9320-4](https://doi.org/10.1007/s10569-010-9320-4)

21. G. Sindoni, D. Grassi, A. Adriani, A. Mura, M. L. Moriconi, B. M. Dinelli, G. Filacchione, F. Tosi, G. Piccioni, A. Migliorini, F. Altieri, F. Fabiano, D. Turrini, R. Noschese, A. Cicchetti, S. Stefani, S. J. Bolton, J. E. P. Connerney, S. K. Atreya, F. Bagenal, C. Hansen, A. Ingersoll, M. Jansen, S. M. Levin, J. I. Lunine, G. Orton, M. Amoroso, Characterization of the white ovals on Jupiter's southern hemisphere using the first data by Juno/JIRAM instrument. *Geophys. Res. Lett.* 10.1002/2017GL072940 (2017). [doi:10.1002/2017GL072940](https://doi.org/10.1002/2017GL072940)
22. D. Grassi, A. Adriani, A. Mura, B. M. Dinelli, G. Sindoni, D. Turrini, G. Filacchione, A. Migliorini, M. L. Moriconi, F. Tosi, R. Noschese, A. Cicchetti, F. Altieri, F. Fabiano, G. Piccioni, S. Stefani, S. Atreya, J. Lunine, G. Orton, A. Ingersoll, S. Bolton, S. Levin, J. Connerney, Preliminary results on the composition of Jupiter's troposphere in Hot Spot regions from the JIRAM/Juno instrument. *Geophys. Res. Lett.* 10.1002/2017GL072841 (2017). [doi:10.1002/2017GL072841](https://doi.org/10.1002/2017GL072841)
23. M. Roos-Serote, S. K. Atreya, M. K. Wong, P. Drossart, On the water abundance in the atmosphere of Jupiter. *Planet. Space Sci.* **52**, 397–414 (2004). [doi:10.1016/j.pss.2003.06.007](https://doi.org/10.1016/j.pss.2003.06.007)
24. R. Jacobson, R. Haw, T. McElrath, P. Antreasian, A comprehensive orbit reconstruction for the Galileo Prime mission in the J2000 system. *Adv. Astronaut. Sci.* **103**, 465–486 (1999).
25. M. Parisi, E. Galanti, S. Finocchiaro, L. Iess, Y. Kaspi, Probing the depth of Jupiter's Great Red Spot with the Juno gravity experiment. *Icarus* **267**, 232–242 (2016). [doi:10.1016/j.icarus.2015.12.011](https://doi.org/10.1016/j.icarus.2015.12.011)
26. J. K. Campbell, S. P. Synnott, Gravity field of the jovian system from Pioneer and Voyager tracking data. *Astrophys. J.* **90**, 364–372 (1985).
27. The JUP230 solution corresponds to the gravity field of Jupiter calculated by R. A. Jacobson in 2003 using Pioneer, Voyager, and Galileo data as released on http://ssd.jpl.nasa.gov/?gravity_fields_op
28. The JUP310 solution corresponds to the gravity field of Jupiter calculated by R. A. Jacobson in 2013 using Pioneer, Voyager, Galileo, and New Horizons data as released on http://ssd.jpl.nasa.gov/?gravity_fields_op
29. N. Nettelmann, A. Becker, B. Holst, R. Redmer, Jupiter models with improved ab initio hydrogen equation of state (H-REOS.2). *Astrophys. J.* **750**, 52 (2012). [doi:10.1088/0004-637X/750/1/52](https://doi.org/10.1088/0004-637X/750/1/52)
30. Y. Kaspi, T. Guillot, E. Galanti, Y. Miguel, R. Helled, W. Hubbard, B. Militzer, S. Wahl, S. Levin, J. Connerney, S. Bolton, The effect of differential rotation on Jupiter's low-degree

- even gravity moments. *Geophys. Res. Lett.* 10.1002/2017GL073629 (2017). doi:10.1002/2017GL073629
31. S. M. Wahl, W. B. Hubbard, B. Militzer, T. Guillot, Y. Miguel, Y. Kaspi, R. Helled, D. D. Reese, N. Movshovitz, E. Galanti, S. Levin, J. Connerney, S. Bolton, Gravity measurements and the role of a dilute core. *Geophys. Res. Lett.* 10.1002/2017GL073160 (2017). doi:10.1002/2017GL073160
32. J. E. P. Connerney, M. Benn, J. B. Bjarno, T. Denver, J. Espley, J. L. Jorgensen, P. S. Jorgensen, P. Lawton, A. Malinnikova, J. M. Merayo, S. Murphy, J. Odom, R. Oliverson, R. Schnurr, D. Sheppard, E. J. Smith, The Juno magnetic field investigation. *Space Sci. Rev.* 10.1007/s11214-017-0334-z (2017). doi:10.1007/s11214-017-0334-z
33. J. E. P. Connerney, M. H. Açuna, N. F. Ness, T. Satoh, New models of Jupiter's magnetic field constrained by the Io Flux Tube footprint. *J. Geophys. Res.* **103**, 11929–11939 (1998). doi:10.1029/97JA03726
34. J. E. P. Connerney, Planetary magnetism. In *Treatise on Geophysics, Volume 10: Planets and Satellites*, G. Schubert, T. Spohn, Eds. (Elsevier, 2015), pp. 195–237; <https://ntrs.nasa.gov/archive/nasa/casi.ntrs.nasa.gov/20150011017.pdf>.
35. R. Smoluchowski, Jupiter's molecular hydrogen layer and the magnetic field. *Astrophys. J.* **200**, L119–L121 (1975). doi:10.1086/181911
36. W. J. Nellis, S. T. Weir, A. C. Mitchell, Metallization and electrical conductivity of hydrogen in Jupiter. *Science* **273**, 936–938 (1996). doi:10.1126/science.273.5277.936 [Medline](#)
37. M. French, A. Becker, W. Lorenzen, N. Nettelmann, M. Bethkenhagen, J. Wicht, R. Redmer, Ab initio simulations for material properties along the Jupiter adiabat. *Astrophys. J. Suppl. Ser.* **202**, 5 (2012). doi:10.1088/0067-0049/202/1/5
38. T. Guillot, D. J. Stevenson, W. B. Hubbard, D. Saumon, in *Jupiter*, F. Bagenal, T. Dowling, W. B. McKinnon, Eds. (Cambridge Univ. Press, 2004), chap. 3.
39. W. B. Hubbard, B. Militzer, A preliminary Jupiter model. *Astrophys. J.* **820**, 80 (2016). doi:10.3847/0004-637X/820/1/80
40. Y. Miguel, T. Guillot, L. Fayon, Jupiter internal structure: The effect of different equations of state. *Astron. Astrophys.* **596**, A114 (2016). doi:10.1051/0004-6361/201629732
41. T. R. Hanley, P. G. Steffes, B. M. Karpowicz, A new model of the hydrogen and helium-broadened microwave opacity of ammonia based on extensive laboratory measurements. *Icarus* **202**, 316–335 (2009). doi:10.1016/j.icarus.2009.02.002
42. K. Devaraj, P. G. Steffes, D. Duong, The centimeter-wavelength opacity of ammonia under deep jovian conditions. *Icarus* **241**, 165–179 (2014). doi:10.1016/j.icarus.2014.06.017
43. A. Bellotti, P. G. Steffes, G. Chinsomboon, Laboratory measurements of the 5-20 cm wavelength opacity of ammonia, water vapor and methane under simulated conditions for

- the deep jovian atmosphere. *Icarus* **280**, 255–267 (2016).
[doi:10.1016/j.icarus.2016.07.013](https://doi.org/10.1016/j.icarus.2016.07.013)
44. E. C. Morris, R. W. Parsons, Microwave absorption by gas mixtures at pressures up to several hundred bars. I. Experimental technique and results. *Aust. J. Phys.* **23**, 335–349 (1971).
 45. V. R. Eshleman, G. L. Tyler, G. E. Wood, G. F. Lindal, J. D. Anderson, G. S. Levy, T. A. Croft, Radio science with Voyager at Jupiter: Initial Voyager 2 results and a Voyager 1 measure of the Io torus. *Science* **206**, 959–962 (1979). [doi:10.1126/science.206.4421.959](https://doi.org/10.1126/science.206.4421.959) [Medline](#)
 46. M. K. Bird, S. W. Asmar, J. P. Brenkle, P. Edenhofer, O. Funke, M. Pätzold, H. Volland, Ulysses radio occultation observations of the Io plasma torus during the Jupiter encounter. *Science* **257**, 1531–1535 (1992). [doi:10.1126/science.257.5076.1531](https://doi.org/10.1126/science.257.5076.1531) [Medline](#)
 47. S. W. Asmar, J. W. Armstrong, L. Iess, P. Tortora, Spacecraft Doppler tracking: Noise budget and accuracy achievable in precision radio science observations. *Radio Sci.* **40**, n/a (2005). [doi:10.1029/2004RS003101](https://doi.org/10.1029/2004RS003101)
 48. J. A. Barnes, A. R. Chi, L. S. Cutler, D. J. Healey, D. B. Leeson, T. E. McGunigal, J. A. Mullen, W. L. Smith, R. L. Sydnor, R. F. C. Vessot, G. M. R. Winkler, Characterization of frequency stability. *IEEE Trans. Instrum. Meas.* **IM-20**, 105–120 (1971).
[doi:10.1109/TIM.1971.5570702](https://doi.org/10.1109/TIM.1971.5570702)
 49. W. M. Kaula, *Theory of Satellite Geodesy: Applications of Satellites to Geodesy* (Blaisdell, Waltham, MA, 1966).
 50. G. Bierman, *Factorization Methods for Discrete Sequential Estimation* (Academic Press, 1997).
 51. A. Milani, G. Gronchi, *Theory of Orbit Determination* (Cambridge Univ. Press, 2010).
 52. S. V. Gavrilov, V. N. Zharkov, Love numbers of the giant planets. *Icarus* **32**, 443–449 (1977). [doi:10.1016/0019-1035\(77\)90015-X](https://doi.org/10.1016/0019-1035(77)90015-X)
 53. M. Parisi, E. Galanti, S. Finocchiaro, L. Iess, Y. Kaspi, Probing the depth of Jupiter’s Great Red Spot with the Juno gravity experiment. *Icarus* **267**, 232–242 (2016).
[doi:10.1016/j.icarus.2015.12.011](https://doi.org/10.1016/j.icarus.2015.12.011)
 54. D. H. Atkinson, J. B. Pollack, A. Seiff, The Galileo Probe Doppler Wind Experiment: Measurement of the deep zonal winds on Jupiter. *J. Geophys. Res.* **103**, 22911–22928 (1998).
 55. D. Grassi, A. Adriani, M. L. Moriconi, N. I. Ignatiev, E. D’Aversa, F. Colosimo, A. Negrão, L. Brower, B. M. Dinelli, A. Coradini, G. Piccioni, Jupiter’s hot spots: Quantitative assessment of the retrieval capabilities of future IR spectro-imagers. *Planet. Space Sci.* **58**, 1265–1278 (2010). [doi:10.1016/j.pss.2010.05.003](https://doi.org/10.1016/j.pss.2010.05.003)

56. C. R. Rodgers, *Inverse Methods for Atmospheric Sounding: Theory and Practice* (World Scientific, 2000).
57. P. G. J. Irwin, N. A. Teanby, R. de Kok, L. N. Fletcher, C. J. A. Howett, C. C. C. Tsang, C. F. Wilson, S. B. Calcutt, C. A. Nixon, P. D. Parrish, The NEMESIS planetary atmosphere radiative transfer and retrieval tool. *J. Quant. Spectrosc. Radiat. Transf.* **109**, 1136–1150 (2008). [doi:10.1016/j.jqsrt.2007.11.006](https://doi.org/10.1016/j.jqsrt.2007.11.006)
58. A. Kylling, K. Stamnes, S.-C. Tsay, A reliable and efficient two-stream algorithm for spherical radiative transfer: Documentation of accuracy in realistic layered media. *J. Atmos. Chem.* **21**, 115–150 (1995). [doi:10.1007/BF00696577](https://doi.org/10.1007/BF00696577)
59. A. P. Showman, T. E. Dowling, Nonlinear simulations of Jupiter's 5-micron hot spots. *Science* **289**, 1737–1740 (2000). [10.1126/science.289.5485.1737](https://doi.org/10.1126/science.289.5485.1737) [Medline](#)
60. R. Hueso, A. Sánchez-Lavega, Motions in hot spot-plume regions using Voyager images. *Icarus* **136**, 353–357 (1998). [doi:10.1006/icar.1998.6018](https://doi.org/10.1006/icar.1998.6018)
61. D. Choi, A. P. Showman, A. R. Vasavada, A. A. Simon-Miller, Meteorology of Jupiter's equatorial hot spot and plumes from Cassini. *Icarus* **223**, 832–843 (2013). [doi:10.1016/j.icarus.2013.02.001](https://doi.org/10.1016/j.icarus.2013.02.001)